nature communications

Article

https://doi.org/10.1038/s41467-025-67948-2

Metallic tellurium for p-type contacts of two-dimensional $MoTe_2$ field-effect transistors

Received: 24 July 2025

Accepted: 12 December 2025

Published online: 13 January 2026

Check for updates

Yuhan Zhu[1,2], Feng Wang[1,2] ✉, Shuhui Li[1], Chen Shen[3], Yuchen Cai[4], Tao Yan[1,2], Fuyuan Zhang[1,5], Yanrong Wang[6], Xueying Zhan[1], Kai Xu[7], Hao Wang[3] ✉, Hongbin Zhang[3], Zhenxing Wang[1,2,5] ✉ & Jun He[2,4] ✉

While significant progress has been made in the fabrication of n-type contacts for two-dimensional field-effect transistors (2D FETs), the development of high-performance p-type counterparts using compatible techniques remains insufficient to realize competitive complementary circuits. Here, we demonstrate the growth of metallic-phase tellurium (m-Te) on $MoTe_2$ via evaporation as an efficient p-type contact. The atomic arrangement at the Te/$MoTe_2$ interface stabilizes m-Te under ambient conditions, forming an atomically sharp van der Waals gap with optimal band alignment and suppressed metal-induced gap states. Combined with hole doping and tellurium vacancies compensation, the interface enables barrier-free hole injection. Bilayer $MoTe_2$ FETs employing m-Te contacts achieve a contact resistance as low as 1.6 kΩ μm, an on-state current up to 124 μA μm^{-1}, and a maximum on/off ratio of 10^7, which are among the best values obtained for p-type 2D FETs. Our work unveils metallic-phase chalcogen as a promising approach for contact optimization.

The atomically thin bodies and dangling bond-free surfaces of two-dimensional (2D) semiconductors make them promising candidates for advanced logic devices[1–3]. However, these features also pose challenges for realizing high-performance field-effect transistors (FETs) using standard fabrication processes. One key issue is the high contact resistance. Charge carriers transport across metal-semiconductor interfaces via diffusion, thermionic emission, thermionic field emission, and pure field emission (tunneling), depending on the barrier height and width at the interface[4]. In silicon (Si) technology, ion implantation is commonly employed to heavily dope the regions beneath contacts, narrowing the barrier and facilitating low-resistance tunneling contacts[5]. Nevertheless, the high-energy impacts involved in this process can irreversibly damage the crystal structure of 2D materials[6,7], rendering it unsuitable for 2D devices.

From the perspective of barrier height, simply selecting a metal with work function matching the semiconductor's band edge (i.e., metals with low/high work functions for n/p-type contacts) is insufficient to achieve ohmic contact. This is because metal-induced gap states (MIGS) and/or defect states at the contact interface can pin the actual Fermi level within the band gap, resulting in a high charge injection barrier and a severe deviation from the Schottky-Mott rule[8,9]. One might expect that 2D semiconductors could avoid this issue because of their dangling-bond-free van der Waals (vdW) surfaces. However, interactions involving the *d* orbitals between the transition metal atoms in transition metal dichalcogenides (TMDs) and electrode metals lead to serious MIGS[10,11]. Additionally, lattice damage on atomically thin 2D bodies during metal deposition further exacerbates Fermi level pinning[12], thus degrading contact performance. Recently, significant progress has been made in n-type 2D semiconductors using

[1]CAS Key Laboratory of Nanosystem and Hierarchical Fabrication, National Center for Nanoscience and Technology, Beijing, P. R. China. [2]Center of Materials Science and Optoelectronics Engineering, University of Chinese Academy of Sciences, Beijing, P. R. China. [3]Technical University of Darmstadt, Darmstadt, Germany. [4]Key Laboratory of Artificial Micro- and Nano-structures of Ministry of Education, School of Physics and Technology, Wuhan University, Wuhan, P. R. China. [5]School of Advanced Interdisciplinary Sciences, University of Chinese Academy of Sciences, Beijing, P. R. China. [6]Institute of Semiconductors, Henan Academy of Sciences, Zhengzhou, P. R. China. [7]Hangzhou Global Scientific and Technological Innovation Center, School of Micro-Nano Electronics, Zhejiang University, Hangzhou, China. ✉e-mail: wangf@nanoctr.cn; haowang@tmm.tu-darmstadt.de; wangzx@nanoctr.cn; He-jun@whu.edu.cn

semimetal contacts. With energy alignments, suppressed MIGS, and moderate evaporation temperatures, bismuth (Bi) and antimony (Sb) have shown contact performance surpassing even advanced Si technologies[8,9].

In contrast, progress in p-type 2D FETs has lagged far behind, primarily for two reasons. First, achieving p-type ohmic contacts requires the use of high-work-function metals such as gold (Au), platinum (Pt), and palladium (Pd). These heavy metals tend to generate intense thermal radiation during deposition[12]; their high momentum resulting from high atomic mass transfers substantial kinetic energy to the surface atoms of 2D semiconductors, exacerbating lattice damage (Supplementary Fig. 1) and Fermi level pinning[6]. Although lowering deposition temperatures has yielded some improvement, the reported contact resistance for monolayer WSe_2 remains as high as 229 kΩ μm[12]. Second, unlike n-type contacts, suitable high-work-function semimetals for p-type contacts are lacking. While a low contact resistance of 0.75 kΩ μm on WSe_2 has been achieved using Sb/Pt contact, it relies on a MoO_x capping layer for p-type doping and exhibits ambipolar transport behavior[13]. Therefore, developing a compatible and scalable strategy to improve p-type 2D FET contacts remains an urgent challenge.

Here, we demonstrate the growth of metallic tellurium (m-Te) with a monoclinic $P2_1$ phase on $MoTe_2$, which serves as a promising p-type electrical contact for 2D FETs. The nearly perfect match of interplanar/atom spacing between m-Te (021) and $MoTe_2$ ($\bar{1}100$) planes enables the stabilization of m-Te under ambient conditions. The interface is atomically sharp with a vdW gap of 0.162 nm (surface to surface)/0.332 nm (atom to atom). First-principles calculations indicate that the work function of m-Te is basically aligned with the valence band maximum of $MoTe_2$ with mild MIGS and a negligible tunneling barrier. Besides, m-Te p-dopes the underlying $MoTe_2$ and compensates for its tellurium vacancies, thereby enhancing p-type characteristics. The m-Te-contacted bilayer $MoTe_2$ transistors show a pure p-type transport behavior with a low contact resistance of 1.6 kΩ μm, an on-state current of up to 124 μA μm^{-1}, and a maximum on/off ratio of 10^7. These parameters are among the highest-performance p-type 2D FETs reported to date. Our work presents a promising direction for optimizing contacts of 2D semiconductors via in-situ metallic chalcogens growth.

Results

Main concept of m-Te for p-type contacts of 2D FETs

The key to achieving low-resistance p-type contacts for 2D FETs lies in identifying contact metals with aligned energy levels and a weak Fermi pinning effect. Here, we propose an m-Te as an effective p-type contact for 2H $MoTe_2$. $MoTe_2$ is an ambipolar 2D semiconductor that exhibits p-type dominated transport properties through contact and thickness engineering[14]. As a transition metal chalcogenide (TMD), each vdW layer of $MoTe_2$ consists of a Mo atomic layer sandwiched between two Te atomic layers (Fig. 1a). Each Mo atom exhibits a trigonal prismatic coordination with six surrounding Te atoms, forming triangular chalcogen prisms at both ends. These structural units establish a periodic vdW surface potential landscape (Fig. 1b). The lowest and second-lowest energy positions are located above the centers of hexagonal hollow sites and directly above the Mo atoms, respectively, exhibiting a periodicity that matches the equilibrium vdW interaction radius of chalcogen atoms (Fig. 1a, b). This unique configuration enables the controlled introduction of an additional metallic chalcogen layer[15].

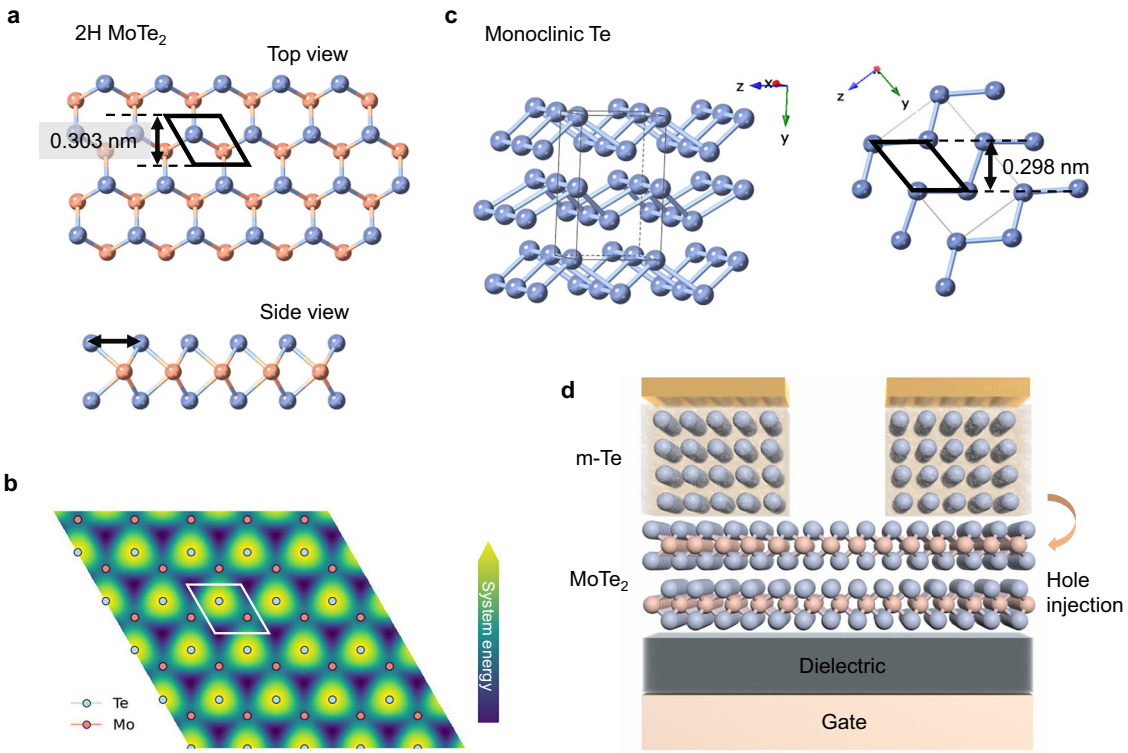

Fig. 1 | Schematic illustration of m-Te induced by 2H $MoTe_2$ as a p-type electrical contact. a Top and side views of the $MoTe_2$ crystal structure. The black rhombus shows the periodicity of the hexagonal hollow sites of the $MoTe_2$ lattice. The black arrows mark the spacing of $MoTe_2$ ($\bar{1}100$) planes. **b** Top view of the energy landscape of Te atoms on $MoTe_2$. The system energy for Te adsorption was obtained by comparing the total energies of $MoTe_2$ with a single Te adatom placed at different surface sites. The white rhombus shows the periodicity of the hexagonal hollow sites, i.e., the lowest energy positions, of the $MoTe_2$ lattice. **c** Crystal structure of m-Te in a three-dimensional manner (left) and along [100] direction (right). The black rhombus and arrows show the periodicity of Te atoms and the spacing of (021) planes. **d** Schematic drawing of the bilayer $MoTe_2$ transistor structure using m-Te as p-type contacts. Blue and coral spheres: Te and Mo atoms.

Given that the fully filled *d*-orbitals of chalcogens can alleviate the possibility of MIGS generation[10], this induced metallic chalcogen layer has the potential to serve as a good electrical contact for the TMDs.

Elemental Te typically adopts a trigonal phase consisting of helical chains along the c-axis ($P3_121$ or $P3_221$ space groups, depending on chirality), and has a band gap of 0.33 eV under ambient conditions (Supplementary Fig. 2). However, under high pressure (~45 kbar), Te transforms into a monoclinic metallic phase with a space group of $P2_1$ (Fig. 1c, d, and Supplementary Fig. 3)[16,17]. This phase exhibits a layered, buckled structure resembling black phosphorous but lacks its armchair-chain configuration. Instead, each Te atom forms covalent bonds with four neighbors within zigzag (020) planes, which are stacked together by weak vdW force (the detailed unit parameters can be found in Supplementary Fig. 3e,f).

Notably, the interplanar spacing of m-Te (021) planes matches that of 2H $MoTe_2$ ($\bar{1}100$) planes, with aligned unit sizes (Fig. 1a, c). Thus, 2H $MoTe_2$ can be potentially employed as a natural template for m-Te growth. Moreover, m-Te has a work function slightly below the valence band minimum (VBM) of 2H $MoTe_2$[18], rendering it a promising p-type contact for $MoTe_2$ FETs (Fig. 1d).

Structure and mechanism of m-Te for p-type contacts of 2D FETs

15/80 nm Te/Au contacts were deposited on $MoTe_2$ following the above hypothesis, with 15 nm Te serving as a hole injection buffer layer (see Methods). The surface potential induction effect of $MoTe_2$ was first verified by scanning electron microscopy (SEM) characterization of the Te buffer morphology (Supplementary Fig. 4). The Te film shows a textured morphology with three dominant orientations on $MoTe_2$ with different thicknesses (Supplementary Fig. 5), which is distinct from the randomly distributed spherical clusters on silicon dioxide (SiO_2), indicating the possibility of van der Waals oriented growth[19,20].

The interface structure of Te/$MoTe_2$ was further investigated using cross-sectional high-angle annular dark-field scanning transmission electron microscopy (HAADF-STEM) (Fig. 2a, b and Supplementary Fig. 6). Te forms clean and atomically sharp vdW contacts with $MoTe_2$, showing an interfacial spacing of 0.162 ± 0.01 nm (surface to surface)/0.332 ± 0.01 nm (atom to atom) (Fig. 2b)—smaller than typical vdW gaps in temperature-controlled deposition[12] or transfer contacts[6]. The interplanar distances of Te and $MoTe_2$ along the interface are 0.310 nm and 0.316 nm, corresponding to $P2_1$ Te (021) planes and $MoTe_2$ ($\bar{1}100$) planes, respectively (denoted by the top blue and bottom orange lines in Fig. 2b). The lattice mismatch, defined as $|d_{(021)} - d_{(\bar{1}100)}|/d_{(\bar{1}100)}$, is only ~1.90%. More importantly, since $P2_1$ Te belongs to the monoclinic crystal system, Te (021) planes and $MoTe_2$ (0001) planes are non-orthogonal. Therefore, the (021) interplanar distance differs from that of the evaporated Te atoms at the Te/$MoTe_2$ interface (0.316 nm, marked by the top orange line in Fig. 2b). This value is identical to $MoTe_2$ ($\bar{1}100$) planes spacing, manifesting the potential landscape of $MoTe_2$ surface as shown in Fig. 1b.

Multiple characterizations confirmed the existence of monoclinic $P2_1$ Te, including the selected-area electron diffraction (SAED) of $P2_1$ Te (021) planes (Fig. 2c, d and Supplementary Fig. 7a, b), fingerprint X-ray diffraction (XRD) peaks of $P2_1$ Te (021) and (110) planes at 2θ = ~ 30.09° and 30.42° (Fig. 2e), and the fast Fourier transform (FFT) of the cross-sectional STEM images (Supplementary Fig. 7c, d). This finding is intriguing because: (i) $P2_1$ Te, typically requiring high-pressure synthesis[16], now can be obtained through simple evaporation, and (ii) $P2_1$ Te ($02\bar{1}$) planes, rather than its vdW (001) planes, align parallel to 2H $MoTe_2$ (0001) planes. Both are attributed to the lattice matching as discussed below.

The experimental diffraction pattern (Fig. 2c) matches well with theoretical predictions (Fig. 2d). The circle where the hexagonal pattern corresponding to $MoTe_2$ ($\bar{1}100$) planes (dashed mark) is located intersects with a monoclinic pattern marked with solid lines corresponding to m-Te (021) planes. Two features should be noted. First, the spots share almost identical radius (~0.298 nm for m-Te and ~0.303 nm for $MoTe_2$, corresponding to a mismatch of ~1.65%), aligning well with the STEM results. Second, the three sets of m-Te patterns bisect the hexagonal $MoTe_2$ pattern with a 60° inter-angle (Supplementary Fig. 7a), consistent with the three-fold orientation observed in SEM.

To investigate the preferred atomic configurations of evaporated tellurium atoms on $MoTe_2$ and their structural stabilization mechanism, density functional theory (DFT) calculations were carried out. Figure 2f shows the top and side view of the relaxed heterostructure (see methods), which agrees with the cross-sectional STEM results: evaporated tellurium atoms at the interface are located directly above the hexagonal hollow sites of $MoTe_2$ surface with matched crystal spaces along the y direction (~0.3056 nm for both m-Te and $MoTe_2$). The structure of Te in the heterostructure (Supplementary Fig. 8a–d) shows slight distortion from pristine m-Te (Fig. 1c and Supplementary Fig. 3), indicating the interaction between Te and $MoTe_2$. Due to the spacing mismatch along the x direction, the Te atoms cannot align with the centers of the hexagonal hollow sites. Instead, they sit above positions between the hexagonal centers and Mo atoms in $MoTe_2$, corresponding to the lowest and second-lowest energy sites (Fig. 1b). The atomic alignment of Te on $MoTe_2$, combined with the threefold symmetry of $MoTe_2$ (0001) plane, explains both the three main orientations of Te in SEM and SAED pattern.

We also calculated the formation energy of monoclinic $P2_1$ Te and trigonal $P3_121$ Te on $MoTe_2$ (see detailed crystal structures in Supplementary Fig. 8). Although $P3_121$ is the stable phase under ambient conditions, the formation energy of $P2_1$ Te is lower than that of $P3_121$ phase on $MoTe_2$ (Fig. 2g). This confirms that the lattice induction from $MoTe_2$ stabilizes the metallic phase.

This growth strategy for chalcogen allotropes can be extended to other chalcogen-TMD systems. For instance, $R\bar{3}$ Se consisting rhombohedral Se_6 rings can be achieved by depositing selenium on WSe_2 (Supplementary Fig. 9). Analogously, previous studies have demonstrated the formation of metallic S in S/MoS_2 heterostructures[15]. These findings suggest that such in-situ unusual-phase growth could serve as a versatile platform for exploring intriguing transport characteristics in chalcogen/TMD vdW heterostructures.

To evaluate the feasibility of m-Te as a p-type contact for $MoTe_2$ FETs, electronic band structures of m-Te and $MoTe_2$ were investigated, respectively. First-principles calculations and a clear Fermi step beyond the zero binding energy in Ultraviolet Photoelectron Spectroscopy (UPS) confirm the metallic nature of $P2_1$ Te (Fig. 3a, the reciprocal primary cell is shown in Supplementary Fig. 7e; UPS results are shown in Supplementary Fig. 11d), consistent with previous reports[16], fulfilling the fundamental requirement for electrical contacts. In addition, the Kelvin probe force microscopy (KPFM) results in Supplementary Fig. 10 indicate that the electric potential of m-Te is higher than that of $MoTe_2$. The potential difference between m-Te/$MoTe_2$ heterostructure and $MoTe_2$ is approximately 45 meV. UPS results in Supplementary Fig. 11a-c indicate the work function of m-Te/$MoTe_2$ heterostructure is 4.57 eV, larger than the Fermi level of free-standing $MoTe_2$ (4.3 eV), confirming the positive charge transfer from m-Te to $MoTe_2$. The band offset of m-Te, 2H $MoTe_2$ and m-Te/$MoTe_2$ was further investigated by first-principles calculations in Supplementary Fig. 11e.

After in contact with m-Te, the density of states (DOS) of $MoTe_2$ (Fig. 3b, lower panel) exhibits minor modifications compared to its pristine counterpart (Fig. 3b, upper panel), in stark contrast to TMD/traditional metal contacts (such as Au, In, Pt, Pd)[21], where high density of MIGS appears within the bandgaps. The alleviation of in-gap MIGS in the case of m-Te contact indicates a lower possibility of Fermi-level pinning. We zoomed in on DOS of the band gap in Supplementary Fig. 12 and found that the band gap of $MoTe_2$ in contact with m-Te becomes narrower than that of the pristine one, and the metal-induced states lie within the band as an extension of band edge. Specifically, the

https://doi.org/10.1038/s41467-025-67948-2

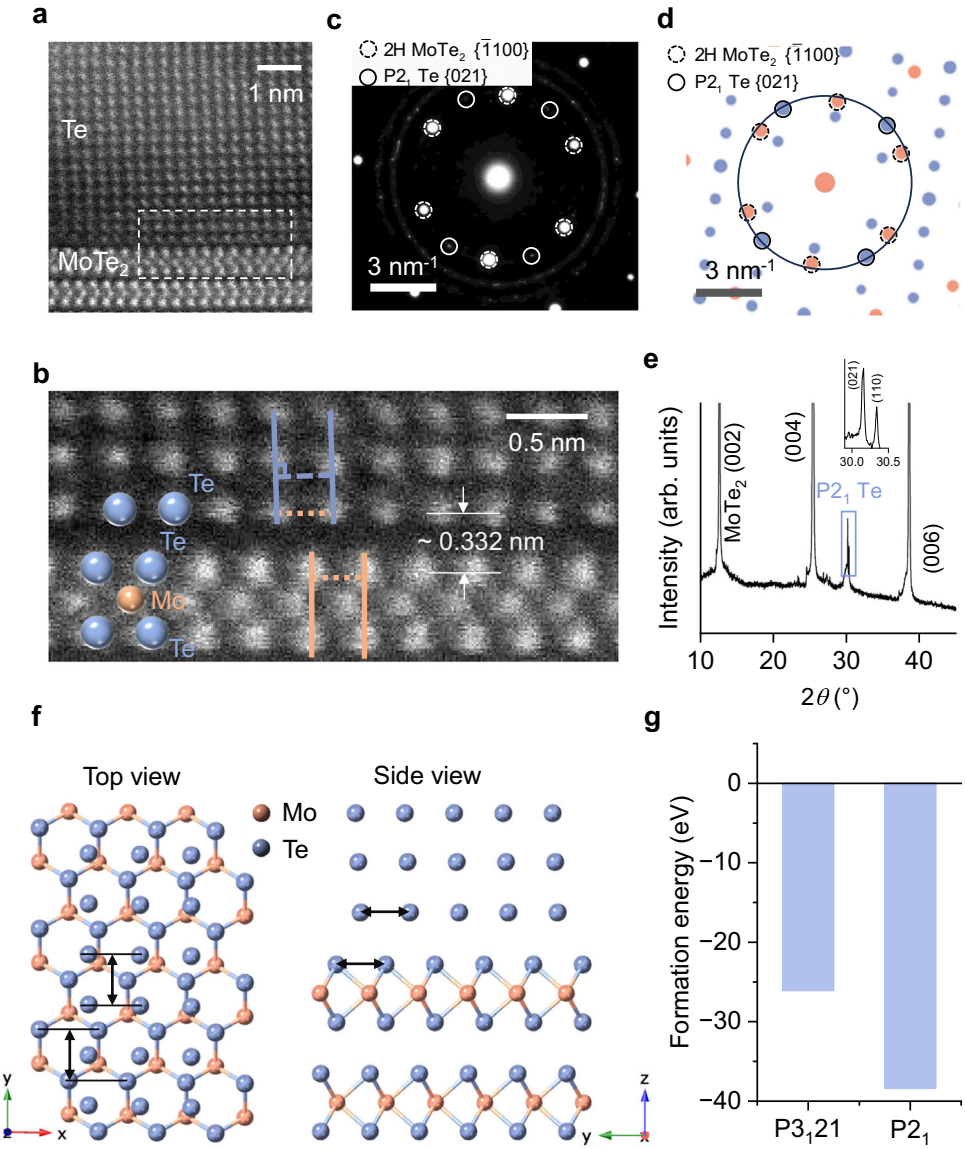

Fig. 2 | Structure of $P2_1$ Te/2H $MoTe_2$ heterostructure. a,**b** Atomic resolution images of Te on $MoTe_2$. **a** High-angle annular dark field (HAADF) scanning transmission electron microscope (STEM) image showing a clean interface between Te and $MoTe_2$. Scale bar, 1 nm. b Enlarged dashed rectangle region from (**a**) in which Mo and Te atoms are visible. Scale bar, 5 Å. The plane and atom distances of Te are shown in blue and orange lines. The plane distance in $MoTe_2$ is also indicated by orange lines. **c** Selected area electron diffraction (SAED) patterns of $MoTe_2$ and Te circled in dotted and solid lines, respectively. Scale bar, 3 nm^{-1}. The predominant diffraction dots of polycrystal Te are circled. **d** Simulated diffraction pattern of $MoTe_2$ and monoclinic Te along [001] and [100], respectively. Scale bar, 3 nm^{-1}. **e** X-Ray Diffraction (XRD) pattern of $MoTe_2$ covered by evaporated Te. Inset, enlarged XRD pattern of $P2_1$ Te. **f** Top and side views of the relaxed Te/$MoTe_2$ structure from density functional theory (DFT) calculation. The black arrows mark the spacing of $MoTe_2$ ($\bar{1}100$) planes and of Te (021) planes, respectively. **g** The formation energy of $P3_121$ Te and $P2_1$ Te on $MoTe_2$.

valence band edge of Te-contacted $MoTe_2$ composed mainly of Mo d_{z^2} and Te p_z bends shifts upwards compared with pristine $MoTe_2$, and the conduction band edge of it composed mainly of Te p_z shifts downwards. As a result, the Fermi level (E_F) of the heterojunction approaches the VBM of $MoTe_2$, accompanied by electron depletion of it (Fig. 3c and Supplementary Fig. 11f). The above clearly demonstrates the p-type doping effect of m-Te on $MoTe_2$, which remains robust even in the presence of donor-like Te vacancies in $MoTe_2$ as shown in Fig. 3c (defect densities: $3.281 \times 10^{13}\,cm^{-2}$ and $6.562 \times 10^{13}\,cm^{-2}$ corresponding to one vacancy and two vacancies per supercell, respectively) -a common occurrence in practical $MoTe_2$ samples[22].

Furthermore, Te exhibits a tellurium-vacancy compensation effect on $MoTe_2$. The DOS analysis shows that the energy of defect states shifts toward the VBM with reduced density after heterostructure formation (Supplementary Fig. 13a, b), facilitating electron acceptance and enhancing p-type characteristics. Electron spin resonance (ESR) measurements at 92 K provide direct evidence of this compensation effect, showing diminished Te-vacancy-related resonance ($g \approx 2.004$) following Te deposition[23] (Fig. 3d). This compensation stems from interfacial charge transfer enabled by the favorable band alignment between m-Te and $MoTe_2$.

Besides, the tunneling barrier between m-Te and $MoTe_2$ was calculated to possess a width (w_t) of 1.27 Å and a height (Φ_t) of 2.95 eV (Supplementary Fig. 11g), both smaller than those of semimetal/MoS_2 n-type contacts[8,9]. These results theoretically support the favorable conditions of m-Te as p-type contacts of $MoTe_2$.

The p-type doping effect of m-Te on $MoTe_2$ was systematically verified through multiple characterizations. Raman spectroscopy

https://doi.org/10.1038/s41467-025-67948-2

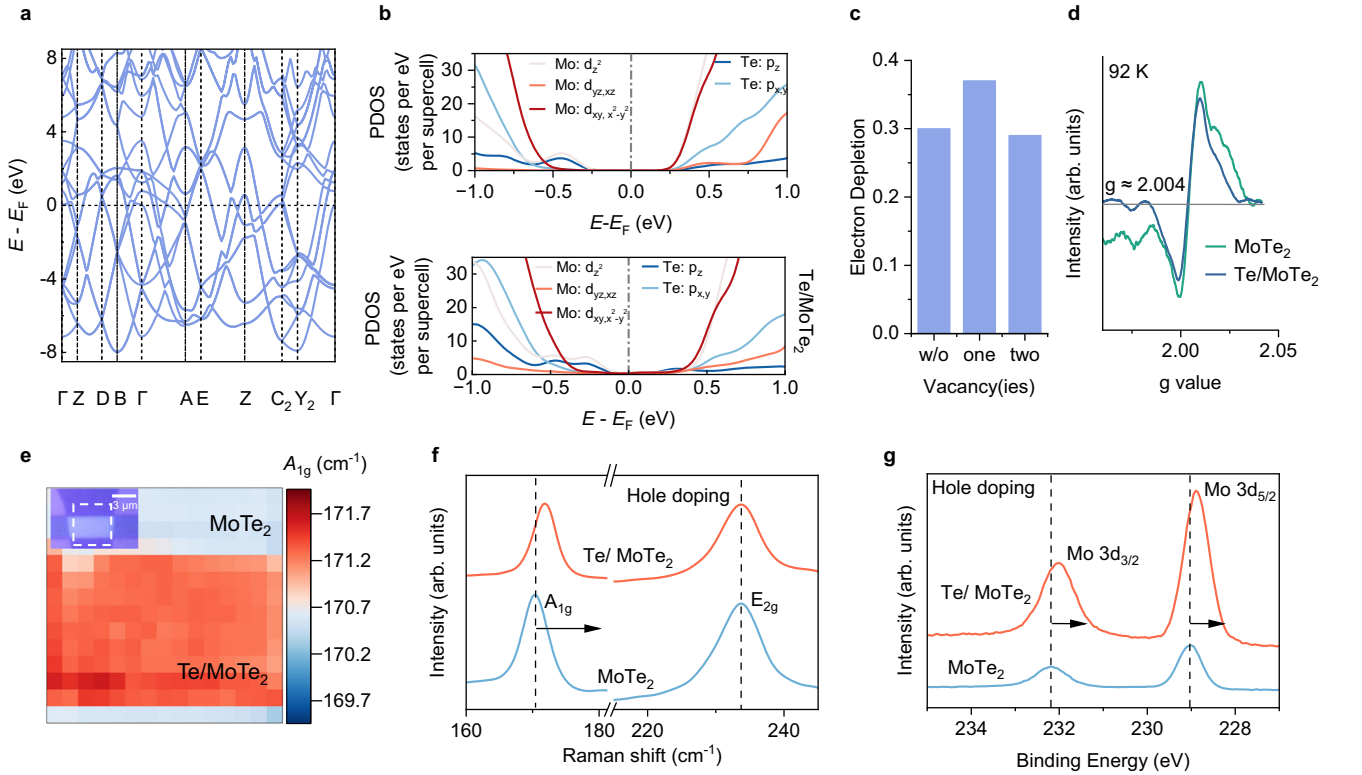

Fig. 3 | Mechanism of m-Te as p-type contacts for $MoTe_2$. **a** Band structure of $P2_1$ Te. **b** Projected density of states (PDOS) of free-standing $MoTe_2$ (upper panel), where the Fermi level (E_F) lies around the middle of the band gap, and of $MoTe_2$ in contact with m-Te (lower panel). Mo d_{z^2} and Te p_z orbitals of $MoTe_2$ extend into the band gap after $MoTe_2$ is in contact with m-Te. The E_F of the system approaches the valence band maximum of $MoTe_2$. **c** Electron loss of $MoTe_2$ with different numbers of Te vacancies per supercell after being in contact with Te. **d** Electron spin resonance (ESR) results of $MoTe_2$ and $Te/MoTe_2$. The g value determines at which magnetic field the resonance occurs for a fixed microwave frequency. The signal at g around 2.004 corresponds to unpaired electrons from Te vacancies. **e** Raman mapping of A_{1g} peak positions from $MoTe_2$ to $Te/MoTe_2$ and then to $MoTe_2$. Inset: the corresponding optical microscope image of the heterostructure. Scale bar, 3 μm. **f, g** Raman (**f**) and X-ray photoelectron spectroscopy (XPS) (**g**) spectra of pure $MoTe_2$ and $Te/MoTe_2$. The arrows indicate the shift directions of the spectra after introducing Te.

revealed a uniform ~1.5 cm^{-1} blueshift in the A_{1g} mode of m-Te-contacted bilayer $MoTe_2$ (Fig. 3e, f and Supplementary Fig. 14a, b), confirming moderate p-doping, while the unchanged E_{2g} mode indicated negligible interfacial strain. Note that no widening occurred of the A_{1g} full width at half maximum (FWHM) (Supplementary Fig. 14c, d), distinct from Pt/Pd-contacted $MoTe_2$ (Supplementary Fig. 1), indicating negligible surface damage of m-Te contacted $MoTe_2$. The A_{1g} peak even became narrower after Te deposition. This might be related to the compensatory effect we mentioned above. Besides, X-ray photoelectron spectroscopy (XPS) measurements demonstrate consistent 180 meV redshifts in both Mo $3d_{3/2}$ and Mo $3d_{5/2}$ peaks (Fig. 3g), with analogous shifts observed in m-Te $3d_{3/2}$ and Te $3d_{5/2}$ peaks (Supplementary Fig. 15), collectively revealing a lowering of the Fermi level when $MoTe_2$ is in contact with m-Te[24–26]. KPFM analysis further corroborated these findings, showing a significant surface potential reduction in Te-contacted regions (Supplementary Fig. 16).

Furthermore, we analyzed the interaction between interfacial atoms based on the results of energy loss spectroscopy (EELS) and crystal orbital Hamilton population (COHP) calculations. In the EELS experiment, we observed that the edge shape, i.e., the curve slope of interfacial $MoTe_2$ Layer 1 in EELS profile (Supplementary Fig. 17) of the m-Te/$MoTe_2$ scenario is unparallel to those of the layers away from the interface, which refers to changed electronic structures, quite different from the parallel scenario in van der Waals Pt contact[12]. Thus, the p-type doping and defect compensation effects brought by m-Te create distinct electronic environments at the interface, making the first-layer Te in $MoTe_2$ different from that of the inner parts. However, no obvious energy shift was observed, indicating that no new bonds were formed at the interface. In addition, to further assess the interfacial Te–Te interaction strength, −COHP (minus Crystal Orbital Hamilton Population) curves and −ICOHP (integrated −COHP) were further computed. In Supplementary Fig. 18, the −COHP curves show that the Te–Te interaction is much weaker than the Mo–Te interaction within 2H $MoTe_2$ and the Te–Te interaction within m-Te, manifesting −COHP values hovering close to zero, with only small oscillations. This sharp contrast is then quantified by −ICOHP values, i.e., 0.15 eV per bond for interfacial Te–Te pairs, 2.23 eV per bond for $MoTe_2$ Mo–Te pairs, and 1.12 eV for Te–Te pairs in m-Te.

High-performance $MoTe_2$ p-FETs with metallic Te contacts

Finally, we investigate the electrical performance of bilayer $MoTe_2$ FETs employing m-Te as contacts. The analysis of the thickness of $MoTe_2$ can be seen in Supplementary Fig. 19 and Supplementary Fig. 20. Figs. 4a, b show the transfer curve (i.e., source-drain current vs. gate voltage, I_{ds}-V_{gs}) and output curves (i.e., source-drain current vs. source-drain voltage, I_{ds}-V_{ds}), respectively. Notably, the device exhibits primarily p-type transport behavior with excellent linearity at full-range gate voltages (Supplementary Fig. 21) and at temperatures from 100 K to 300 K (Supplementary Fig. 22a–k), confirming the formation of high-quality p-type ohmic contacts. Furthermore, the devices maintained stable transfer characteristics after 10 months of storage, proving the long-term reliability of m-Te contacts for p-type $MoTe_2$ FETs (Supplementary Fig. 22i); and the m-Te contacts remain stable after 300 °C annealing and 10^3 s prolonged operation, as shown in Supplementary Fig. 23 and Supplementary Fig. 24. Devices with variable channel lengths (L_{ch}) were fabricated (Fig. 4c inset) on uniform

https://doi.org/10.1038/s41467-025-67948-2

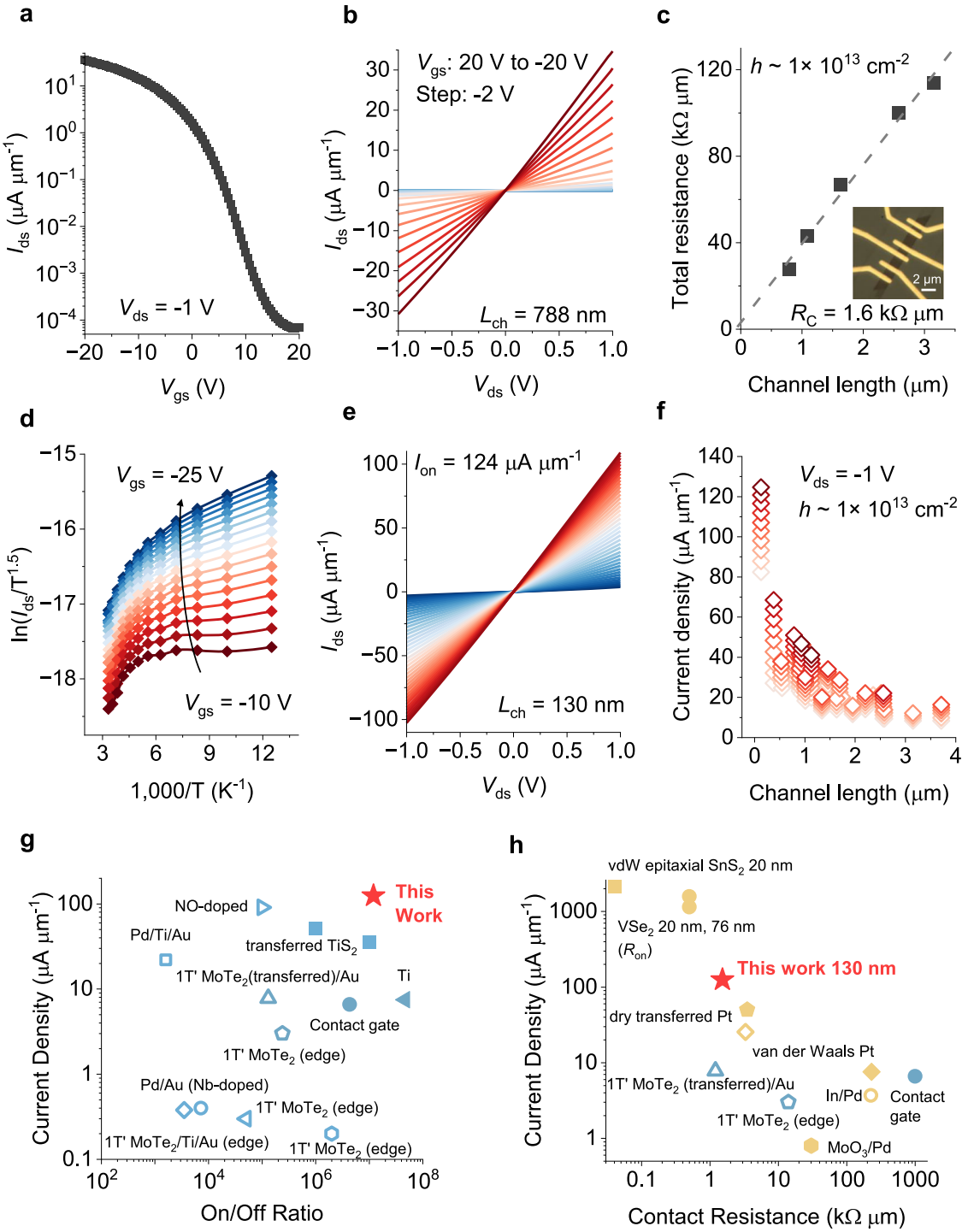

Fig. 4 | Electrical properties and benchmark of bilayer $MoTe_2$ with m-Te contacts. a,b P-type bilayer $MoTe_2$ FET electrical characteristics. Transfer curves (**a**) of bilayer $MoTe_2$ with m-Te contacts showing pure p-type device characteristics. Linear output characteristics (**b**) of bilayer $MoTe_2$ with Te contacts. V_{gs}, V_{ds} and I_{ds} refer to gate voltage, bias voltage and current density, respectively. W = 2.63 μm, L = 788 nm. **c** Transfer length method (TLM) results of bilayer $MoTe_2$ with m-Te contacts when the hole density is around 1 × 10^{13} cm^{-2}. The inset shows the optical microscope image of the TLM device. Scale bar, 2 μm. **d** Arrhenius plots of the Te–$MoTe_2$ at V_{gs} from -10 V to -25 V and V_{ds} of -1 V. T is temperature, with the unit being Kelvin. The barrier for the Te–$MoTe_2$ interface is negligible. **e** I_{ds}–V_{ds} curves of the Te-bilayer $MoTe_2$ (exfoliated) field-effect transistor (FET) with L_{ch} of 130 nm. V_{gs}: 0 V to -40 V, step: -1 V. I_{on} is the current density at minimum V_{gs} (-40 V here) and V_{ds} of -1 V. **f** Statistics of I_{on} for 25 Te-contacted bilayer $MoTe_2$ transistors. Data are extracted at the hole density around 1×10^{13}cm^{-2} and at the same V_{ds} of -1 V. **g, h** Benchmark of current density and on/off ratio of p-type $MoTe_2$ FETs (g) and of current density and contact resistance of p-type FETs based on $MoTe_2$ FETs and undoped WSe_2 FETs (h), with values reported in the literature using different methods. The blue and yellow marks represent the performance of p-type $MoTe_2$ FETs[42–52] and WSe_2 FETs[7,12,28,31,32,53–55], respectively. The symbols for solid and hollow, respectively, represent devices with 1-2 layers and three or more layers. All current densities are collected at V_{ds} of -1 V.

$MoTe_2$ strips and the transfer-length method (TLM) was employed to quantitatively determine the contact resistance (R_C). It is worth noting that the contact resistance can generally be divided into the intrinsic part that cannot be controlled by the gate and the junction part that can be controlled by the gate[27]. Both of these parts contribute to the contact resistance. Although the TLM method cannot provide the origin and mechanism of the contact resistance, it can still offer a benchmark reference for the total interface resistance. Remarkably, the bilayer $MoTe_2$ devices show R_C as low as 1.6 kΩ μm at a carrier density (p_{2D}) of ~1.0×10^{13} cm^{-2} (Fig. 4c), with consistent performance observed in multiple devices (Supplementary Fig. 25).

The excellent p-type contact properties originate from the ideal band alignment between m-Te and $MoTe_2$, as confirmed by Schottky barrier analysis. Unlike conventional Schottky contacts that exhibit negative slopes in Arrhenius plots ($\ln(I_{ds}/T^{1.5})$ vs. 1,000/T, where T is temperature), m-Te/$MoTe_2$ FETs consistently show positive slopes when the device is turned on, providing direct evidence for barrier-free hole injection (Fig. 4d, Supplementary Fig. 26 and Supplementary Fig. 27). For the details of the Arrhenius curves, please refer to Methods. The absence of an effective hole barrier suggests weak Fermi-level pinning, which can be attributed to the following factors: (1) $MoTe_2$ remains intact after Te evaporation, ruling out the introduction of interfacial defect states; (2) The vdW gap between m-Te and $MoTe_2$ minimizes the overlap between the orbitals of m-Te and $MoTe_2$ and the MIGS induced by m-Te are negligible; (3) The tellurium-vacancy compensation effect of m-Te above $MoTe_2$ can suppress the defect-induced gap states.

A 130 nm L_{ch} bilayer $MoTe_2$ FET was fabricated to further increase the on-state current (I_{on}). The device shows good linear output curves with an I_{on} achieved 124 μA $μm^{-1}$ at a V_{ds} of -1 V (Fig. 4e). Figure 4f presents the statistics of I_{on} measured on 25 $MoTe_2$ devices with channel length at a p_{2D} of around 1×10^{13} cm^{-2}, indicating good repeatability of the high-performance p-type contacts using metallic Te (see detailed characteristics of each device in Supplementary Fig. 28).

We finally benchmark our devices with the state-of-the-art 2D p-type FETs based on $MoTe_2$ (blue) and undoped WSe_2 (orange) (Fig. 4g, h). Given that few-layer 2D semiconductor devices generally exhibit lower performance compared to those based on multilayer counterparts, we distinguish the data between 1-2 layers (solid) and multilayer devices (hollow). It is worth noting that all $MoTe_2$ samples used in this work were exfoliated from bulk crystals, which are closer to intrinsic semiconductors compared to those grown by chemical vapor deposition (CVD). Our devices yield one of the highest current densities among $MoTe_2$ transistors and an on/off ratio reaching ~1.2×10^7, which is comparable to 100 nm-channel WSe_2/Pt devices (CVD-grown) on 5 nm SiO_2[28]. Although the NO doping method has improved the p-type contact, the thermal stability of which still needs to be enhanced[29,30]. To the best of our knowledge, the achieved contact resistance of 1.6 kΩ·μm represents one of the lowest reported values for undoped mono-/bilayer p-type $MoTe_2$. Compared to metal transfer or CVD-grown epitaxial approaches[31,32], our direct thermal evaporation of Te offers superior compatibility with existing silicon technologies since the transfer process is omitted and there is no need to consider the etching issue after m-Te growth. As shown in Supplementary Fig. 29, the m-Te contact strategy also has the potential to be extended to the fabrication of devices on large-scale $MoTe_2$, facilitating subsequent integration.

Discussion

In summary, we have demonstrated that in-situ metallic Te can serve as a promising p-type electrical contact for $MoTe_2$ FETs. This strategy yields a low contact resistance of 1.6 kΩ μm, an on-state current of up to 124 μA $μm^{-1}$, and an on/off ratio of 10^7 in bilayer $MoTe_2$ transistors, which are among the highest-performance p-type 2D FETs reported to date. The success of this approach stems from three key factors. First, the nearly equal atomic spacing at m-Te/$MoTe_2$ interface stabilizes m-Te under ambient conditions, bypassing the need for high-pressure synthesis. Second, with aligned energy level, moderate orbital hybridization, hole doping and tellurium-vacancy compensation effect, the interface shows minor MIGS and a minimal hole injection barrier. Third, direct thermal evaporation of Te avoids lattice damage and strong Fermi-level pinning typically associated with high-energy metal deposition. This work not only presents a key step forward in p-type 2D electronics but also establishes a promising approach for vdW engineering through in-situ chalcogens on TMDs.

Methods

Device fabrication

Al_2O_3 deposited on highly doped silicon through atomic layer deposition (ALD) was used as a back-gate substrate. The process was performed at 150 °C with a growth rate of 1.4 Å per cycle. Bilayer $MoTe_2$ samples were mechanically exfoliated from bulk crystals and identified by optical contrast. Before exfoliating $MoTe_2$, Al_2O_3 substrates were cleaned by O_2 plasma (20 sccm, 30 W, 5 s) to increase the exfoliation yield. The 15/80 nm Te/Au electrodes were made by electron-beam lithography (EBL) and thermal evaporation. Then, $MoTe_2$ FETs were annealed at 100 °C for 30 min in an inert gas environment to enhance the contact performance.

We noticed that p-type 2D semiconductors are sensitive to electron beam lithography (EBL) acceleration voltage, which may explain the persistent challenges in achieving high-performance p-type 2D contacts. Although high acceleration voltage (100 kV) enables high resolution and good pattern fidelity (Supplementary Fig. 30a, d), it simultaneously brings a certain degree of n-type doping on 2D semiconductors. As shown in Supplementary Fig. 30, bilayer $MoTe_2$ FETs with Te contacts exposed at 100 kV exhibit nonlinear output and n-dominated bipolar transfer characteristics. To mitigate this effect, we employed a low acceleration voltage of 10 kV for all device fabrication in this work, which effectively suppressed electron beam-induced n-type in $MoTe_2$ (Fig. 4a, b). Moreover, the contact areas were exposed using a beam current of 150 pA and an areal dose of 120 in the system to minimize thermal effects and charge accumulation[33].

For TLM devices, $MoTe_2$ was patterned by EBL and etched to a bar geometry by reactive ion etching with CF_4 and O_2 plasma. The subsequent processing steps are the same as for other normal devices.

Note that the process of adding a protective layer actually prolongs the time that $MoTe_2$ exposing to the air or introduces more unstable sources, like water during the deposition of dielectrics. As shown in Supplementary Fig. 31, we observed the performance degradation even in multilayer devices after capping an additional layer of Al_2O_3. Therefore, in this work, the m-Te/$MoTe_2$ FETs did not employ any protective capping layers.

The deposition of m-Te

The Clausius-Clapeyron relation of tellurium's saturated vapor pressure P and temperature T can be written as[34]:

$$lgP(torr) = (10.45 \pm 0.10) - \frac{8021 \pm 71}{T}, T < 723K \quad (1)$$

Before evaporation, the chamber should be vacuumed to 1×10^{-5} ~ 1.8×10^{-5} Pa. After starting to heat the tungsten boat, the evaporation rate is controlled at 0.1 Å s^{-1}, and the chamber soon reaches a stable pressure of about 2.3×10^{-5} Pa (1.73×10^{-7} torr). The "dynamic equilibrium pressure" here is used as the approximation of the saturated vapor pressure of Te powder, then the temperature of 466.0 ± 6.1 K in a tungsten boat can be obtained by the formula. 15 nm Te was deposited onto $MoTe_2$ in 25 min and radiative heating of the 2D materials from the crucible during

metal evaporation was negligible. For Au deposition, the evaporation rate was 0.2 Å s^{-1}.

It is worth noting that lattice matching is the principle for obtaining m–Te on $MoTe_2$, and temperature impacts the m-Te phase formation. To be specific, m-Te used as $MoTe_2$'s contacts is deposited at room temperature, while semiconducting Te can be grown on $MoTe_2$ at high temperature or other substrates like SiO_2/Si without the lattice matching effect.

As shown in Supplementary Fig. 32a, after being deposited at room temperature, Te on $MoTe_2$ and Te on SiO_2/Si show distinct morphology, indicating the significance of lattice match and the inadequacy of SiO_2/Si as the substrate for m-Te growth due to the lack of lattice matching effect. We used to heat the sample stage with $MoTe_2$ on SiO_2/Si attached to 90 °C to deposit Te, and found the same morphology of Te on SiO_2/Si and $MoTe_2$ (Supplementary Fig. 32b). According to the XRD results (Supplementary Fig. 32c), these forms of Te refer to trigonal Te (t-Te), i.e., the semiconducting Te. This may be because heating increases the energy of Te adatoms and overcomes the energy barrier induced by $MoTe_2$ lattice.

Calibration of carrier density

The hole density of $MoTe_2$ FETs was extracted according to:

$$h = \frac{C_{ox}}{q}\left(V_{th} - V_{gs}\right) \tag{2}$$

By evaporating 200 × 200 μm^2 pads of Au on the Al_2O_3 substrates, C_{ox} (F cm^{-2}) was obtained by capacitance measurements using Keysight 1500 and area normalization. According to the transfer characteristics, the V_{th} of each device was extracted in the linear region when V_{ds} = 0.1 V:

$$I_{ds} = \mu C_{ox}\frac{W}{L}(V_{gs} - V_{th})V_{ds} \tag{3}$$

By fitting

$$I_{ds} = aV_{gs} + b, \tag{4}$$

a and b were gained, so

$$V_{th} = -\frac{b}{a} \tag{5}$$

After obtaining C_{ox} and V_{th}, the hole density was derived under certain V_{gs} for each device.

Schottky barrier extraction

The thermionic emission current injected from a metal contact into a 2D channel through a Schottky barrier can be given by the Richardson-Dushman equation:

$$I_{thermo} = A^{*}T^{\alpha}\exp(-\frac{\varphi_B}{k_BT}) \tag{6}$$

where A^* is the Richardson constant, T is the temperature, k_B is the Boltzmann constant, and φ_B is the effective contact barrier height. Considering the energy-independent density of states of a 2D system, α is 3/2 for 2D semiconductors. When a voltage V_{ds} is applied across the Schottky barrier, it modifies the barrier height and the carrier injection process. In a Schottky-barrier FET, the reverse-biased contact accounts for the majority of the voltage drop and plays a critical role in governing the transistor's behavior. The drain current density thermally injected from the metal contact into the 2D channel through such a reverse-biased Schottky barrier can be expressed as:

$$I_{ds} = A^{*}_{2d}T^{1.5}\exp\left(-\frac{\varphi_B}{k_BT}\right)[1 - \exp(-\frac{V_{ds}}{k_BT})] \tag{7}$$

When V_{ds}» k_BT, Eq. (7) can be simplified to:

$$I_{ds} = A^{*}_{2d}T^{1.5}\exp(-\frac{\varphi_B}{k_BT}) \tag{8}$$

In this regime, the effective energy barrier φ_B at a specific V_{gs} can be determined by analyzing the slope of the Arrhenius plots. This is achieved using the following relationship:

$$\ln\left(\frac{I_{ds}}{T^{1.5}}\right) = \frac{-\varphi_B}{k_BT} + c \tag{9}$$

As we can see, the Arrhenius plots of on-state Te-contacted $MoTe_2$ FETs display an opposite trend to the thermionic emission model (Eq. (9)). The absence of a negative slope implies the contact barrier-free nature of the Te–$MoTe_2$ FETs. It is worth noting that the total measured current is set by the series combination of contact-limited injection and channel resistance, which are altered by temperature-dependent scattering mechanisms[35], especially the latter one considering that the channel length of the device used to analyze barrier is 400 nm, manifesting as temperature-dependent current in Supplementary Fig. 26a. This causes the Arrhenius point to exhibit nonlinearity in Supplementary Fig. 26b, c. To make the physical picture clearer, we analyzed the gate-modulated band diagram in Supplementary Fig. 27. After m-Te and $MoTe_2$ contact, the band offset at the interface is fixed. Since the work function of m-Te is higher than the VBM of $MoTe_2$, as gate voltages change, the channel part of $MoTe_2$ can be aligned with respect to the m-Te when the positive gate modulation reaches a certain point, rather than the conventional flat band condition. The "barrier" energy of this pseudo flat-band condition might correspond to the energy required for holes to escape from the potential well at the contact interface.

Measurements

Transport characteristics were measured by applying voltages with the Keysight 1500 semiconductor parameter analyzer system. The low-temperature measurements were performed in a vacuum probe station with liquid nitrogen and a temperature controller.

ESR was tested by Brucker EMXplus-9.5/12. A mass of $MoTe_2$ was exfoliated to a 3 × 7 mm SiO_2/Si substrate and slid to the bottom of the tube for ESR test at 92 K. After the test, $MoTe_2$/SiO_2/Si was vacuumized immediately and ready for 15 nm Te evaporation. Then the ESR test of Te/$MoTe_2$/SiO_2/Si was conducted.

Raman data were collected by 633-nm laser excitation focused through a ×100 objective lens using Renishaw inVia-Qontor. XPS was performed using the Thermo Scientific EACALAB 250Xi. Atomic force microscopy and Kelvin probe force microscopy (KPFM) were performed using the Brucker multimode 8HR. To conduct KPFM, 15 nm Te was evaporated onto exfoliated $MoTe_2$ on PDMS. Then, Te/$MoTe_2$ was transferred to a Au substrate with $MoTe_2$ on the upper side.

DFT calculations

DFT calculations in this work were performed using the Vienna Ab initio Simulation Package (VASP)[36,37]. The Perdew–Burke–Ernzerhof (PBE) functional within the generalized gradient approximation (GGA)[37] was used to describe the exchange-correlation interactions. The projector-augmented wave (PAW)[38] method was adopted, and the kinetic energy cutoff was set to 400 eV. The Brillouin zone was

sampled using the Monkhorst–Pack method[39] with a k-point mesh density of 0.03 $Å^{-1}$. The DFT-D3[40] correction of Grimme with Becke–Johnson (BJ) damping[41] was used to describe the interlayer van der Waals interactions. All structures were fully relaxed. The force and energy convergence criteria were set to 10^{-2} eV/Å and 10^{-5} eV, respectively. The heterostructure was modeled using a slab structure. A vacuum layer of 20 Å was added along the z direction to avoid interactions between periodic images.

Data availability

The Source Data underlying the figures of this study are available with the paper. All raw data generated during the current study are available from the corresponding authors upon request. Source data are provided with this paper.

References

1. Cao, W. et al. The future transistors. *Nature* **620**, 501–515 (2023).
2. Kim, K.-H. & Jariwala, D. Advances in next-generation logic devices with two-dimensional channel materials. *IEEE Nanotechnol. Mag.* **19**, 4–12 (2025).
3. Liu, Y. et al. Promises and prospects of two-dimensional transistors. *Nature* **591**, 43–53 (2021).
4. Heinzel, T. *Mesoscopic Electronics in Solid State Nanostructures*. (Wiley, 2007).
5. Dennard, R. H. et al. Design of ion-implanted MOSFET's with very small physical dimensions. *IEEE J. Solid-State Circuits* **9**, 256–268 (1974).
6. Liu, Y. et al. Approaching the Schottky–Mott limit in van der Waals metal–semiconductor junctions. *Nature* **557**, 696–700 (2018).
7. Jung, Y. et al. Transferred via contacts as a platform for ideal two-dimensional transistors. *Nat. Electron.* **2**, 187–194 (2019).
8. Li, W. et al. Approaching the quantum limit in two-dimensional semiconductor contacts. *Nature* **613**, 274–279 (2023).
9. Shen, P.-C. et al. Ultralow contact resistance between semimetal and monolayer semiconductors. *Nature* **593**, 211–217 (2021).
10. Kim, C. et al. Fermi level pinning at electrical metal contacts of monolayer molybdenum dichalcogenides. *ACS Nano* **11**, 1588–1596 (2017).
11. Gong, C., Colombo, L., Wallace, R. M. & Cho, K. The unusual mechanism of partial fermi level pinning at Metal–MoS_2 interfaces. *Nano Lett* **14**, 1714–1720 (2014).
12. Wang, Y. et al. P-type electrical contacts for 2D transition-metal dichalcogenides. *Nature* **610**, 61–66 (2022).
13. Chou, A.-S. et al. High-Performance Monolayer WSe_2 p/n FETs via Antimony-Platinum Modulated Contact Technology towards 2D CMOS Electronics. in *2022 International Electron Devices Meeting (IEDM)* 7.2.1-7.2.4 (2022). https://doi.org/10.1109/IEDM45625.2022.10019491.
14. Wang, F. et al. Uncovering the conduction behavior of van der waals ambipolar semiconductors. *Adv. Mater.* **31**, 1805317 (2019).
15. Zhu, S. et al. Metallic and highly conducting two-dimensional atomic arrays of sulfur enabled by molybdenum disulfide nanotemplate. *Npj Comput. Mater.* **3**, 1–8 (2017).
16. Aoki, K., Shimomura, O. & Minomura, S. Crystal structure of the high-pressure phase of tellurium. *J. Phys. Soc. Jpn.* **48**, 551–556 (1980).
17. Bridgman, P. W. Polymorphism, principally of the elements, up to 50,000kg/cm^2. *Phys. Rev.* **48**, 893–906 (1935).
18. Michaelson, H. B. The work function of the elements and its periodicity. *J. Appl. Phys.* **48**, 4729–4733 (1977).
19. Li, T. et al. Epitaxial growth of wafer-scale molybdenum disulfide semiconductor single crystals on sapphire. *Nat. Nanotechnol.* **16**, 1201–1207 (2021).
20. Li, H. et al. Controlled synthesis of topological insulator nanoplate arrays on mica. *J. Am. Chem. Soc.* **134**, 6132–6135 (2012).
21. Kang, J., Liu, W., Sarkar, D., Jena, D. & Banerjee, K. Computational study of metal contacts to monolayer transition-metal dichalcogenide semiconductors. *Phys. Rev. X* **4**, 031005 (2014).
22. Cho, S. et al. Phase patterning for ohmic homojunction contact in $MoTe_2$. *Science* **349**, 625–628 (2015).
23. Guo, J. et al. Bimetallic sulfides with vacancy modulation exhibit enhanced electrochemical performance. *Adv. Funct. Mater.* **34**, 2315714 (2024).
24. Han, H.-V. et al. Photoluminescence enhancement and structure repairing of monolayer $MoSe_2$ by hydrohalic acid treatment. *ACS Nano* **10**, 1454–1461 (2016).
25. Nipane, A., Karmakar, D., Kaushik, N., Karande, S. & Lodha, S. Few-layer MoS_2 p-type devices enabled by selective doping using low energy phosphorus implantation. *ACS Nano* **10**, 2128–2137 (2016).
26. Qu, D. et al. Carrier-type modulation and mobility improvement of thin $MoTe_2$. *Adv. Mater.* **29**, 1606433 (2017).
27. Ber, E., Grady, R. W., Pop, E. & Yalon, E. Uncovering the different components of contact resistance to atomically thin semiconductors. *Adv. Electron. Mater.* **9**, 2201342 (2023).
28. Wang, X., Shi, X., Xiong, X., Huang, R. & Wu, Y. BEOL compatible high-performance monolayer WSe_2 pFETs with record G_m=190 μS/μm and I_{on}=350μA/μm by direct-growth on SiO_2 substrate at reduced temperatures. in *2023 International Electron Devices Meeting (IEDM)* 1–4 (2023). https://doi.org/10.1109/IEDM45741.2023.10413833.
29. Lan, H.-Y. et al. Uncovering the doping mechanism of nitric oxide in high-performance P-type WSe_2 transistors. *Nat. Commun.* **16**, 4160 (2025).
30. Cai, J. et al. High-performance complementary circuits from two-dimensional $MoTe_2$. *Nano Lett* **23**, 10939–10945 (2023).
31. Wu, R. et al. Bilayer tungsten diselenide transistors with on-state currents exceeding 1.5 milliamperes per micrometre. *Nat. Electron.* **5**, 497–504 (2022).
32. Zhao, B. et al. Gate-driven band modulation hyperdoping for high-performance p-type 2D semiconductor transistors. *Science* **388**, 1183–1188 (2025).
33. Jiang, J., Xu, L., Qiu, C. & Peng, L.-M. Ballistic two-dimensional InSe transistors. *Nature* **616**, 470–475 (2023).
34. Ubelis, A. P. Temperature dependence of the saturated vapor pressure of tellurium. *J. Eng. Phys.* **42**, 309–315 (1982).
35. Radisavljevic, B. & Kis, A. Mobility engineering and a metal–insulator transition in monolayer MoS_2. *Nat. Mater.* **12**, 815–820 (2013).
36. Kresse, G. & Furthmüller, J. Efficiency of ab-initio total energy calculations for metals and semiconductors using a plane-wave basis set. *Comput. Mater. Sci.* **6**, 15–50 (1996).
37. Perdew, J. P., Burke, K. & Ernzerhof, M. Generalized gradient approximation made simple. *Phys. Rev. Lett.* **77**, 3865–3868 (1996).
38. Blöchl, P. E. Projector augmented-wave method. *Phys. Rev. B* **50**, 17953–17979 (1994).
39. Methfessel, M. & Paxton, A. T. High-precision sampling for Brillouin-zone integration in metals. *Phys. Rev. B* **40**, 3616–3621 (1989).
40. Grimme, S., Antony, J., Ehrlich, S. & Krieg, H. A consistent and accurate ab initio parametrization of density functional dispersion correction (DFT-D) for the 94 elements H-Pu. *J. Chem. Phys.* **132**, 154104 (2010).
41. Grimme, S., Ehrlich, S. & Goerigk, L. Effect of the damping function in dispersion corrected density functional theory. *J. Comput. Chem.* **32**, 1456–1465 (2011).
42. Di, B. et al. High-quality P-type contacts for atomically thin $MoTe_2$ transistors with high-work-function semimetal TiS_2 electrodes. *ACS Appl. Mater. Interfaces* **17**, 25518–25525 (2025).
43. Haratipour, N. & Koester, S. J. Multi-layer $MoTe_2$ p-channel MOSFETs with high drive current. in *72nd Device Research Conference* 171–172 (IEEE, 2014). https://doi.org/10.1109/DRC.2014.6872352.

44. Song, S. et al. Fabrication of p-type 2D single-crystalline transistor arrays with Fermi-level-tuned van der Waals semimetal electrodes. *Nat. Commun.* **14**, 4747 (2023).
45. Sung, J. H. et al. Coplanar semiconductor–metal circuitry defined on few-layer MoTe2 via polymorphic heteroepitaxy. *Nat. Nanotechnol.* **12**, 1064–1070 (2017).
46. Larentis, S. et al. Reconfigurable complementary monolayer $MoTe_2$ field-effect transistors for integrated circuits. *ACS Nano* **11**, 4832–4839 (2017).
47. Kwon, G. et al. Reconfiguring van der Waals metal–semiconductor contacts via selenium intercalation/deintercalation post-treatment. *ACS Nano* **19**, 1619–1629 (2025).
48. He, Q. et al. Molecular beam epitaxy scalable growth of wafer-scale continuous semiconducting monolayer $MoTe_2$ on inert amorphous dielectrics. *Adv. Mater.* **31**, 1901578 (2019).
49. Ma, R. et al. $MoTe_2$ lateral homojunction field-effect transistors fabricated using flux-controlled phase engineering. *ACS Nano* **13**, 8035–8046 (2019).
50. Pan, Y. et al. Precise p-type and n-type doping of two-dimensional semiconductors for monolithic integrated circuits. *Nat. Commun.* **15**, 9631 (2024).
51. Xu, X. et al. Scaling-up atomically thin coplanar semiconductor–metal circuitry via phase engineered chemical assembly. *Nano Lett* **19**, 6845–6852 (2019).
52. Xu, X. et al. Seeded 2D epitaxy of large-area single-crystal films of the van der Waals semiconductor 2H $MoTe_2$. *Science* **372**, 195–200 (2021).
53. Wang, Y. et al. Van der Waals contacts between three-dimensional metals and two-dimensional semiconductors. *Nature* **568**, 70–74 (2019).
54. Wang, J. et al. Steep slope p-type 2D WSe_2 field-effect transistors with van der waals contact and negative capacitance. in *2018 IEEE International Electron Devices Meeting (IEDM)* 22.3.1-22.3.4 (IEEE, 2018). https://doi.org/10.1109/IEDM.2018.8614493.
55. Chen, Y.-H. et al. P-Type ohmic contact to monolayer WSe_2 field-effect transistors using high-electron affinity amorphous MoO_3. *ACS Appl. Electron. Mater.* **4**, 5379–5386 (2022).

Acknowledgements

This work was supported by National Key R&D Program of China (2021YFA1201500 for Z. W.), National Natural Science Foundation of China (Nos. 92464303 for J. H., U24A2055 for Z. W., U24A20302 for F. W., 62374048 for Z. W., 62274046 F. W., 12204122 for S. L., 62574063 for X. Z., 62204217 for K. X.). The authors also gratefully acknowledge the support of Youth Innovation Promotion Association CAS and CAS Key Laboratory of Nanosystem and Hierarchical Fabrication. H. Wang and H. Zhang acknowledge support from the Deutsche Forschungsgemeinschaft (DFG, German Research Foundation) under Project-ID 463184206 – SFB 1548. They also gratefully acknowledge the computing time provided on the high-performance computer Lichtenberg at the NHR Center NHR4CES at TU Darmstadt. The authors thank the Nanofabrication Laboratory at National Center for Nanoscience and Technology for sample fabrication, and Peng Xu, Zhijuan Zhao for the beneficial discussions on XPS characterization and data analysis.

Author contributions

Y.Z. conceived the idea and designed experimental schemes. Y.Z. carried out device fabrication, electrical measurements, materials characterizations and data analysis. Y.Z. and F.W. discussed the data and co-wrote the manuscript in consultation with all the other authors. S.L. assisted in analyzing TEM results. H.W. performed first-principles calculations in consultation with C.S. and H.Z. Y.C., T.Y., F.Z., and Y.W. participated in metal evaporation. F.W., S.L., X. Z., K. X., Z.W., and J.H. provided funding support. Z.W. supervised the project. All authors participated in manuscript revision and refinement.

Competing interests

The authors declare no competing interests.

Additional information

Supplementary information The online version contains supplementary material available at https://doi.org/10.1038/s41467-025-67948-2.

Correspondence and requests for materials should be addressed to Feng Wang, Hao Wang, Zhenxing Wang or Jun He.

Peer review information *Nature Communications* thanks Tuo-Hung Hou, Wenfeng Zhang, and the other, anonymous, reviewer for their contribution to the peer review of this work. A peer review file is available.